

Developing Geostationary Satellite Imaging at Lowell Observatory

Dr. Gerard T. van Belle
Lowell Observatory, Flagstaff, AZ 86001

Abstract

Lowell Observatory operates the Navy Precision Optical Interferometer (NPOI), and owns & operates the Discovery Channel Telescope (DCT). This unique & necessary combination of facilities positions Lowell to develop a robust program of observing geostationary, GPS-plane, and other high-altitude ($\gtrsim 1000$ mi) satellites. NPOI is a six-beam long-baseline optical interferometer, located in Flagstaff, Arizona; the facility is supported by a partnership between Lowell Observatory, the US Naval Observatory, and the Naval Research Laboratory. NPOI operates year-round in the visible with baselines between 8 and 100 meters (up to 432m is available), conducting programs of astronomical research and imaging technology development. NPOI is the only such facility as yet to directly observe geostationary satellites, enabling milliarcsecond resolution of these objects. To enhance this capability towards true imaging of geosats, an ongoing program of facility upgrades will be outlined. These upgrades include AO-assisted 1.0-m apertures feeding each beam line, and new near-infrared instrumentation on the back end. The large apertures will enable ‘at-will’ observations of objects brighter than $m_K = 8.3$ in the near-IR, corresponding to brighter than $m_V = 11.3$ in the visible. At its core, the system is enabled by a ‘wavelength-baseline bootstrapping’ approach discussed herein. A complementary pilot imaging study of visible speckle and aperture masked imaging at Lowell’s 4.3-m DCT, for constraining the low-spatial frequency imaging information, is also outlined.

1 Overall System Architecture

For an integrated solution to the challenge of imaging high-altitude ($\gtrsim 1,000$ miles) satellites, including (but not limited to) geostationary satellites, we are leveraging two major, operational facilities for which Lowell Observatory has privileged access: the observatory’s 4.3-m Discovery Channel Telescope (DCT), and the Navy Precision Optical Interferometer (NPOI). Both of these facilities are operating on-sky *right now* on a daily basis and constitute major infrastructure investments which can be immediately utilized to test and validate many of the techniques necessary for an operational geosat imaging facility.

The system architecture has the following high-level elements: (1) *Optical interferometry*. Spatial resolution in the sub-arcsecond to single-milliarcsecond regime requires an interferometric telescope array. Observing in the ‘optical’ – namely, both visible and near-infrared wavelengths – is required to both achieve the spatial resolution, but also to observe the features of interest on geosats. (2) *Reconfigurable array*. Geosats range in spatial scale from 10-200 milliarcseconds (mas), so adjusting the resolving power of the array through reconfiguration is needed. Additionally, a reconfigurable array provides dense access to $\{u, v\}$ data points for image reconstruction. (3) *Baseline bootstrapping*. The desired resolution element size of 10 cm or smaller can be observed with the longest baselines of an interferometric array, but at low signal-to-noise-ratio (SNR); as such, tracking on short baselines with their high SNR is necessary to coherently lock the long baselines. (4) *Wavelength bootstrapping*. Near-IR fringe tracking (FTK) has two significant (and essential) benefits: first, satellites are brighter in the near-IR than in the visible; second, the lower resolving power of longer wavelength observing means higher SNR for FTK. Both of these benefits increase

the ability of an array to be coherently phased on a satellite for integrating ('staring') at visible wavelengths. (5) *Large apertures*. Satellites are faint relative to the current state-of-the-art in optical interferometry; adaptive-optics (AO) corrected apertures of size ≥ 1.0 m are required. (6) *Complementary single-aperture imaging*. Using the techniques of speckle imaging and non-redundant aperture masking (NRM), Lowell's 4.3 m DCT effectively can operate as a very-short-baseline optical interferometer and serve to constrain image reconstructions. Of these six elements, items 1-3 and 6 have already advanced to on-sky operations.

The NPOI facility has the necessary flexibility for this task of high-altitude satellite imaging and could be optimized in the following ways:

- *Increased aperture size*. NPOI's current 12 cm individual feed apertures are poised to be superseded with the installation of three 1.0 m telescopes. These 'traditional' 1.0 m telescopes will be purchased from PlaneWave Instruments, and are based upon lightweighted fused silica glass mirrors.
- *Adaptive optics*. Turnkey adaptive optics systems are now available commercially, and will be employed to fully utilize the light captured by the 1.0 m telescopes under a variety of seeing conditions. Both natural- and laser-guide-star systems are robust, operating reliably and rapidly [1].
- *Relocatable telescopes*. The 1.0 m telescopes to be added to NPOI will be housed in relocatable enclosures, allowing for a variety of telescope separations.
- *Short baseline stations*. NPOI has stations with separations down to ~ 8 m at the center of the array, and with the complementary use of speckle or NRM at the DCT, spacings below 4.3 m are obtained. Our currently operational stations allow for long baselines to be constructed out of short spacings; additional stations could be commissioned, optimized for the satellite observing case.
- *Baseline bootstrapping*. A paradox of imaging with interferometry is that short baselines are needed to produce fringe visibilities significant enough to track, but long baselines, where fringes are too weak to track, are needed for high resolution imaging. The NPOI is designed to resolve this paradox by building medium to long baselines from a chain of shorter baselines, using the technique of baseline bootstrapping.
- *Wavelength bootstrapping*. Two essential benefits are gained from using near-IR light to fringe track. First, satellites are significantly brighter at near-infrared wavelengths; typical $V - J$ and $V - H$ colors are ~ 3 . [2]. A second benefit in the near-infrared is that, at longer wavelengths, fringe contrast increases. A useful technique is to cophase the array at a high SNR wavelength – in this case, the near-IR – but then take advantage of the cophased array and do imaging at a second, lower SNR wavelength – in this case, the visible. Additionally, the shorter wavelength for imaging provides greater spatial resolution.

Wavelength bootstrapping has already been demonstrated on-sky in a 'short-to-long' fashion at the VLTI, where $2.2 \mu\text{m}$ fringe tracking has increased the sensitivity of the $10 \mu\text{m}$ MIDI instrument by a factor of $20\times$ [3]. However, it is important to note that converse 'long-to-short' technique of imaging from fringe tracking at K -band for V -band imaging has never been demonstrated on sky, and mature development of this technique represents a major technology deliverable of this work.

2 Speckle Imaging & Non-Redundant Aperture Masking

One of the simplest examples of SSA observing desired for geosats, namely “confirming the successful deployment of solar panels”, is already readily obtained from large (> 4 m) single-aperture telescope observations. Using the Differential Speckle Survey Instrument [DSSI, 4], in 2014 we carried out a pilot observational program of geosats and other high-altitude satellites with simultaneous operational wavelengths of 692 nm & 880 nm, resulting in resolving power of 33 mas & 42 mas (the reconstructions from the former are seen in Fig. 1); this is ≈ 7 pixels across large geosats (roughly 6 m resolution at that distance). Although this does not seem like terribly fine resolution, it is indeed sufficient to establish the status of the solar panel deployment on these geosats - not too shabby for an instrument that had a capital investment of $\sim \$200$ k for construction from off-the-shelf components. The sensitivity limit for DSSI is $V \approx 15.5$ on the DCT under the best seeing conditions; secondary objects relative to primaries of this brightness can be detected with a brightness difference of $\Delta m = 3.5$ at separations of 200 mas [5]. Along with the high resolution imaging, a key observational capability demonstrated in this pilot program was the ability to track highly non-sidereal targets with the DCT at altitudes from 10,000 to 25,000 miles.

The closely related technique of non-redundant aperture masking (NRM) on a single telescope is the logical extension of the speckle technique, potentially with improvements in the available contrast ratios over basic speckle interferometry. NRM has been demonstrated on the 8.2-m VLT UT4 telescope as a robust and efficient method for detection of faint stellar companions, and as an approach that improves the effective resolving power of a single aperture from $1.22\lambda/D$ to $\lambda/2D$ [6].

Timeliness of speckle imaging or NRM is related to the operational model of the facility. Given Lowell Observatory’s ownership and direct control over the 4.3-m DCT, significantly more nimble response time is available. The DCT is scheduled on a quarterly basis, and schedule-interrupt arrangements can be made ahead of time for even quicker turnaround if necessary. As an extreme example, the University of Maryland has an agreement with Lowell Observatory to task the DCT on only 15 minutes notice, for capturing follow-up observations of gamma-ray bursters. Observing of this nature typically completes an imaging data cube in a few minutes.

3 Interferometry

3.1 Introduction

The images of geosats from Lowell’s 4.3 m DCT (Fig. 1), with ~ 6 m resolution at red visual wavelengths, and those from the 10 m Keck II Telescope [7], with ~ 5 m resolution at $1.3 \mu\text{m}$,

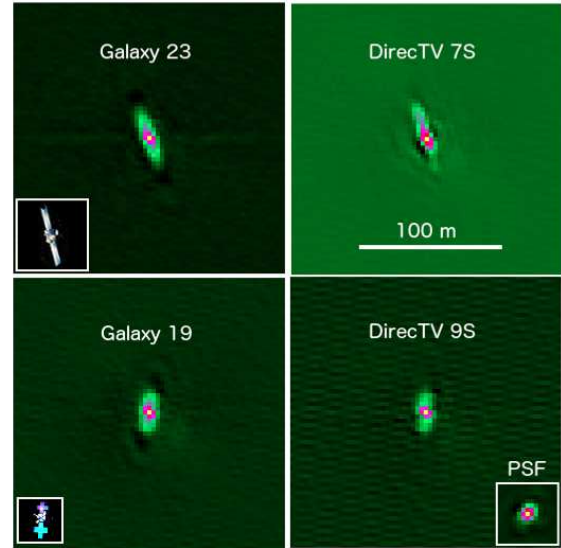


Fig. 1: A montage of speckle images of geosats taken with DSSI@DCT. Galaxy-23, DirecTV-7S, and -9S are all based upon the LS-1300 satellite bus with long, straight solar panels (see upper left inset); Galaxy-19 is also a LS-1300 but with an ‘+’ configuration for its solar panels (lower left inset panel). The point-spread-function of DSSI is seen in the lower right inset panel.

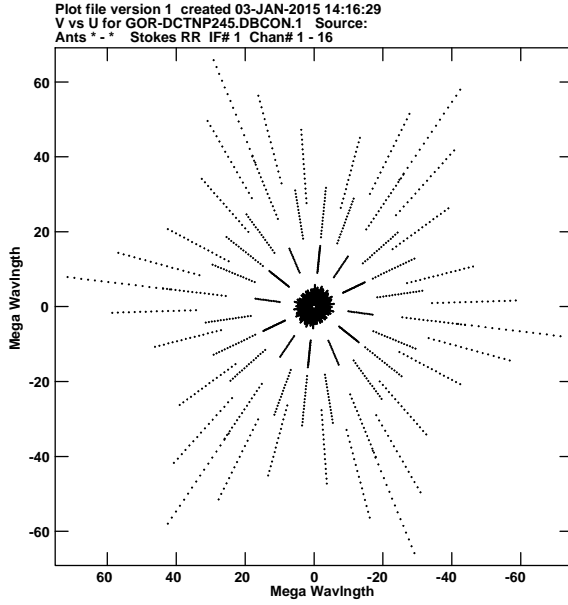


Fig. 2: The $\{u, v\}$ plane coverage of combined DCT and NPOI observations. The central core of data points are the DCT NRM points, with the radial ‘spikes’ of coverage coming from NPOI employing its core short-baseline stations, numbers 2-4-5 for the north, east, and west arms.

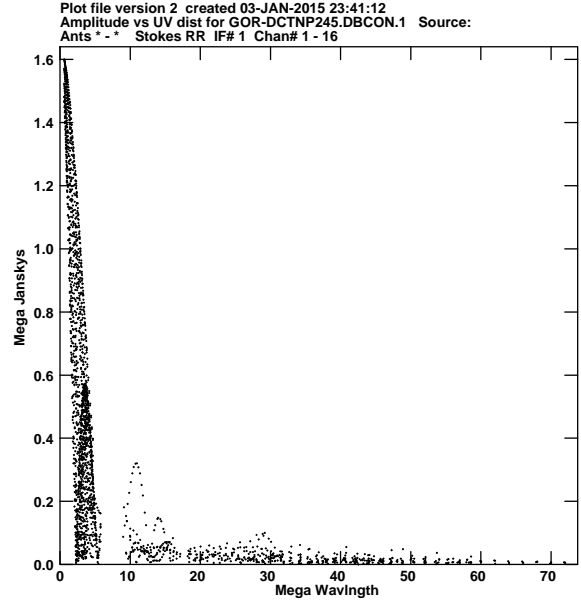


Fig. 3: The expected visibilities from combined DCT and NPOI observations. As with Fig. 2, the central core at low spatial frequencies corresponds to the DCT NRM data, with the high frequency data coming from NPOI.

demonstrate that apertures much larger than 10 m are needed in order to make images of these targets with sub-meter resolution.

An interferometer can overcome these resolution limits by combining light from two or more telescopes to form a virtual aperture with a diameter equal to the separation between telescopes. A detailed exposition on the basics of optical interferometry can be found in our previous proceedings contribution [8]. In short, the relay optics between two telescopes at distance B are adjusted so that the difference ΔD in optical path length from the target through each of the telescopes to the beam combiner is zero, within a tolerance of roughly less than one observational wavelength. Depending on both the length and orientation of the telescope separations, and the target’s size, the interference ‘visibility’ (V) from the light from each pair of telescopes can range from strong to nearly nonexistent.

Atmospheric turbulence significantly changes the effective path lengths through the atmosphere on by many microns on ~ 10 ms timescales. Interferometers track visibility data to measure this effect, and then counteract it by adjusting the relay optics. This adjustment requires that the signal-to-noise ratio $NV^2/2 \gtrsim 1$, where N is the number of photons detected within an atmospheric timescale. The atmospheric timescale is the dominant effect limiting the sensitivity of the interferometer.

The solution to this problem is twofold: observe at longer wavelengths, and lay out the array with chains of telescopes, since V typically increases with λ and B . At longer wavelengths, such as the J -, H -, or K -bands ($\lambda = 1.1\text{--}1.4$, $1.4\text{--}1.8$, $2.0\text{--}2.4 \mu\text{m}$, respectively), the baselines can be two to three times longer before the target is over-resolved ($NV^2/2 < 1$). Correcting the atmospherically induced path length variations using these infrared bands at sufficiently high SNR also corrects them at the visual wavelengths on these longer, higher-resolution baselines, a technique known

as ‘wavelength bootstrapping’. We can also perform a second kind of bootstrapping by using a chain of telescopes. If we use a row of three telescopes with, e.g., 25-m spacing observing in the *J*-band, stabilizing the 25-m baselines between the first and second and between the second and third telescopes automatically stabilizes the 50-m baseline between the first and third telescopes, allowing us to take data on that baseline even though NV^2 on that baseline is too low to directly detect fringes. This ‘baseline bootstrapping’ technique can also be extended to longer chains.

The final challenge is to obtain data over a wide enough range of baseline lengths and orientations to produce a reliable image, also known as ‘ $\{u, v\}$ coverage’ (Fig. 2). In astronomical interferometry, we rely on the rotation of the Earth to assist in changing the baseline orientations, so a Y-shaped configuration with several telescopes along each arm, such as those at the NPOI, is sufficient. For geosat observations, Earth rotation does not help, so an array dedicated to geosat satellite observations requires consideration of a flexible configuration that provides more baseline orientations.

3.2 Baseline-Wavelength Bootstrapping

The combination of baseline and wavelength bootstrapping can be combined into ‘baseline-wavelength bootstrapping’. This combination allows high-resolution observations of extended objects using LBOI. Both the baseline and wavelength bootstrapping aspects of this technique has already been demonstrated separately, at NPOI and two other facilities (CHARA, VLTI). The combined baseline-wavelength bootstrapping technique is robust from a theoretical standpoint but remains untested on the sky.

A criticism that has been leveled against baseline-wavelength bootstrapping is the claim that it will not scale well to targets that are heavily resolved, i.e., those targets whose gross angular size, θ_0 , is many times the desired resolution, θ_{\min} , of the longest baseline. The root of the claim is that the ratio of the longest baseline to the short baselines used for bootstrapping, B_{\max}/B_{boot} , must be $\simeq \theta_0/\theta_{\min}$ because the short baselines must be short enough to produce trackable fringes from the large-scale structure of the target, while the longest baselines must resolve small-scale structure at the desired high resolution. Thus if 25cm resolution is desired on a 10m target, $B_{\max}/B_{\text{boot}} \simeq 40$. This criticism claims that the accumulation of phase errors across 40 steps of bootstrapping will render the technique unworkable.

This critique is invalid for systems that satisfy the parameters of geosat imaging because it overlooks three factors that make baseline-wavelength bootstrapping such a practical, powerful combination. First, the ‘wavelength’ aspect of the bootstrapping from infrared to visible wavelengths can increase B_{boot} by factors from 3 to 6. Wavelength bootstrapping entails tracking fringes in the infrared *H*- ($1.6\mu\text{m}$) or *K*- ($2.2\mu\text{m}$) bands in order to stabilize the fringes in the visual

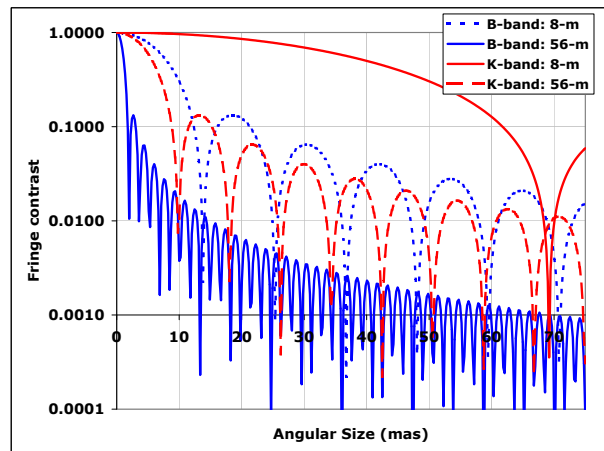


Fig. 4: Visibilities expected from objects of increasing gross size, as a function of wavelength and bootstrapping versus imaging baseline (8m / 56m). As a rough rule-of-thumb, *K*-band fringe contrast at the ~ 5 - 10% level dictates the maximum gross projected size of the object for fringe tracking purposes ($\sim 60\text{mas}$); the number of *B*-band fringe contrast ‘bumps’ inside that envelope correspond roughly to the number of imaging resolution elements (~ 40).

bands (0.4 to 1.0 μm). Because resolution scales inversely with wavelength, B_{boot} at K -band can be $\simeq 5$ times longer than B_{boot} at 0.4 μm , reducing the number of bootstrapping effects by the same factor. Fig. 4 illustrates the concept: with $B_{\text{boot}} = 8\text{m}$ observing at K band (solid red line), the fringe contrast for a $\theta_0 = 40\text{mas}$ ($= 200\text{rad} = 7\text{m}$ at GEO) target is $V \simeq 0.5$. Bootstrapping eight stations together, (i.e. seven 8 m spacings for $B_{\text{max}} = 56\text{m}$) and observing at 0.4 μm produces $V = 0.4$ fringes at resolution $\theta_{\text{min}} = 1\text{mas}$ ($= 5\text{rad} = 17\text{cm}$ at GEO). While the fringe-tracking SNR requirements significantly increase with long-wavelength bootstrapping for short-wavelength imaging, we will show in the next section that these are not insurmountable.

Second, we take advantage of the fact that geosats are significantly brighter in the near IR than at visible wavelengths [$m_V - m_K \simeq 3; 2$].

Third, geosatellite targets have more small-scale structure than the uniform-disk targets implicitly invoked in the critique. The target used in this estimate of this section is a uniform disk, the worst-case scenario. Because these targets are more complex, they produce higher visibility fringes at a given resolution than would a uniform disk with the same overall size (Fig. 5). The result is that the short bootstrapping baselines B_{boot} can be longer than the length $B = \lambda/\theta_0$ that the critique would claim.

A baseline-wavelength bootstrapping demonstration will demonstrate this at NPOI.

An additional, *necessary* benefit of bootstrapping is that image information from baselines that are short, long, and all lengths in-between is captured, allowing for non-aliased image reconstruction; avoiding baseline bootstrapping fundamentally limits the ability to reconstruct images, due to the missing mid-length baselines.

3.3 Sensitivity Limit: Fringe Tracking and Adaptive Optics

The tracking of interference fringes is at the heart of any interferometric system, particularly one peering through the Earth's turbulent atmosphere, so a detailed examination of the performance of such a technique is warranted. For an on-sky source of magnitude m_λ , the number of detected photons per integration frame per aperture is:

$$N_1 = F_{\lambda,0} 10^{-m_\lambda/2.5} \pi (D_1/2)^2 t_0 V_{\text{obj}}^2 T Q (\Delta\lambda/\lambda_c) / s_1 \quad (1)$$

where $F_{\lambda,0}$ is the source flux for a zero-magnitude star at the bandpass λ ; D_1 is the diameter of aperture 1; t_0 is the integration time; V_{obj}^2 is the object visibility; T is the throughput to the detector; Q is the detector quantum efficiency; $\Delta\lambda/\lambda_c$ is the fractional bandpass for the band in question; and s_1 is the number of beam splits for recombination, which in the case of pairwise combination (for nearest-neighbor fringe tracking) is 2. A similar calculation for the second aperture produces a value for N_2 . The integration time t_0 is matched to the expected coherence time for the observational wavelength; in the case of V -band observations, t_0 is expected to be (on reasonable nights) 5ms, and scales as $\lambda^{6/5}$.

The relevant noise has 3 sources: thermal, sky, and read noise. The detected thermal background photons per integration frame per aperture, B_T , and sky background S can be computed as well:

$$B_T = t_0 Q e (\Delta\lambda/\lambda_c) P, \text{ with } P = \frac{2hc^2}{\lambda^5} \frac{1}{e^{hc/\lambda k_B T} - 1}; \quad S = t_0 Q e (\Delta\lambda/\lambda_c) T A \quad (2)$$

where e is the entendue (simply 1 in this case), and P is the familiar Planck function, including the Planck constant h , Boltzmann constant k_B , ambient temperature T , and speed of light c ; A is the air glow rate: for V, J, H, K bands, respectively, is 0, 910, 9700 and 14000 counts/frame. Additionally the count rate due to read noise is $R = 4 \times \text{rn}^2$. Thus, the total noise N_n and signal-to-noise SNR

are

$$N_n = \sqrt{N_1 + \frac{B_T + S}{s_1} + N_2 + \frac{B_T + S}{s_2} + R}, \quad SNR = \frac{4}{\pi} \frac{\sqrt{2N_1N_2\sqrt{St_1St_2}}}{N_n} \quad (3)$$

where St_x is the Strehl ratio for aperture x ; the Strehl is a measurement of the goodness of wavefront quality for a given aperture, ranging from 0 (fully aberrated) up to 1 (unaberrated), scaling roughly as the rms deviation σ of the wavefront phase over the aperture ($\sigma^2 = \langle (\phi - \bar{\phi})^2 \rangle$), $St \approx e^{-\sigma^2}$ [9, 10]. We adopt here the published performance numbers of the Robo-AO laser-guide-star adaptive optics (LGS-AO) system [1] as an existence proof of turnkey LGS-AO; namely $St=26\%$ at 762nm, LGS wavelength of 355nm, a limiting magnitude of $m_V < 16$ and highly efficient operations (<1 minute acquisition time). As with coherence time, the Strehl ratio is expected to scale as $\lambda^{6/5}$, for $St_B=14\%$ and $St_K=93\%$ at B - and K -band, respectively.

Read noise numbers are set to performance seen in the visible for detector systems commonly available (both avalanche photo diodes and electron-multiplying CCD cameras), which are quite good ($<1e^-$). In the near-infrared, in both K - and H -band, some of the best performance available is found with the First Light C-Red One camera, with its notable near-IR performance ($3e^-$ single correlated double read) from its use of the revolutionary Saphira e-APD detector. However, our baseline for immediate implementation of testing wavelength-baseline bootstrapping is a far less expensive (by about $10\times$) InGaAs-based camera with $\sim 35e^-$ read noise, which carries with it a secondary limitation of no K -band sensitivity.

For a given SNR target, we can solve Equations 1 through 3 for m_λ to establish a limiting astronomical magnitude, accounting for detector performance issues (particularly read noise), background (which becomes an issue only at K -band), atmosphere (including single-aperture Strehl ratio and integration time).

We set that SNR target to 3 when considering our long imaging baseline; this in turn sets the fringe-tracking SNR , which has to increase upwards due to two factors. First, fringe tracking errors scale linearly with λ [11]; for going from B -band to H - & K -bands, this corresponds to a factor of 3.6 & $4.9\times$. Second, the same errors accumulate as the square root of the number of baselines (\sqrt{N}), which corresponds to factors of 1.73 , 2.45 , and $2.83\times$ for 3-, 6-, and 8-way systems, respectively.

Given this computational framework, we can compute the limiting magnitudes for two architectures: the current 6×12 cm NPOI (Table 1), and an upgraded 3×1.0 m facility, for the cases of H -band fringe tracking, as well as B -band stabilized fringe integration cases with long synthetic coherence times (~ 1.5 sec), on a 60 mas target with 8 m short baseline spacing. As seen in the final line of Table 1, a limiting magnitude of our 3-way large-aperture architecture is $m_H=8.3$, which corresponds to $m_V \simeq 11.7$ given the very red satellite colors noted above; this limit also agrees well

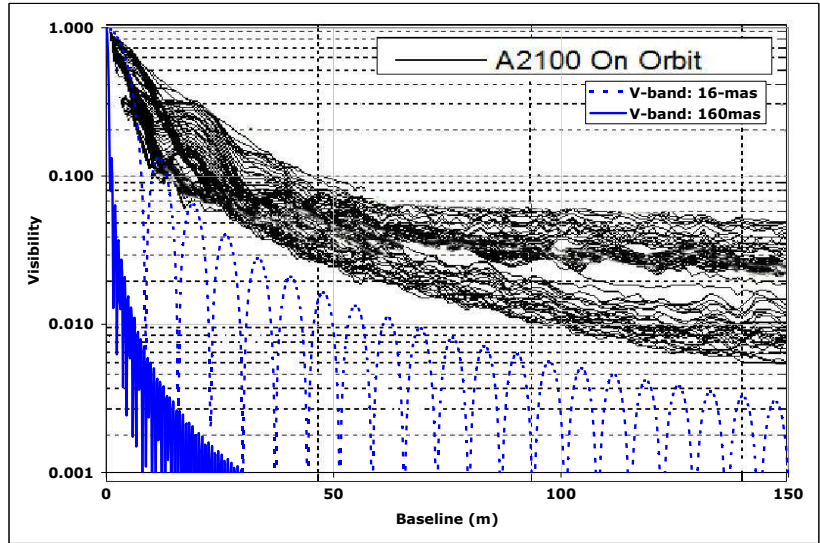


Fig. 5: Visibilities as a function of baseline length at 550nm generated from an A2100 satellite model (black), along with uniform disks of sizes consistent with the major and minor axis sizes of an A2100 (blue).

with the m_B limit also presented in the table. Substantial further benefits can be had in upgrading our detector from H - to K -band operation with a First Light C-Red One camera; notably, the limiting magnitude improves by roughly one magnitude due to the superior read noise performance, and the longer wavelength operation for fringe tracking carries with the benefits noted in §3.2.

3.4 NPOI Status

NPOI is an operational long-baseline optical interferometer, combining up to six beams from independent telescopes. The current small (12 cm) apertures have been used for development of a high-precision astrometric catalog [12], world-first interferometric observations of geosats [13, 14], along with scientific investigations [15, 16, 17, 18]. Recent technical developments include a new six-way beam combiner [19], and a updated instrument back end that provides multi-baseline bootstrapping and coherent integration of fringe visibilities [20, 21]. A detailed instrument paper [22] and a recent update [23] are available.

In FY17 we will be doing a project to add three 1.0 m telescopes to the NPOI facility. Each of these telescopes will be equipped with adaptive optics, and will be relocatable from compact spacings (~ 8 m) out to the ends of each vacuum arm for a full 432 m baseline. An InGaAs near-IR fringe tracker will also be installed to stabilize B - and V -band fringes for the existing imagers.

4 Summary

Key high-altitude satellite imaging technologies will be demonstrated through the addition of large apertures and near-IR fringe-tracking hardware to the existing infrastructure of NPOI, with its sensitivity limits for stellar test sources noted in Table 1. In particular, NPOI is uniquely positioned for immediate demonstration of the necessary system engineering, integration & test, and on-sky demo of the baseline-wavelength bootstrapping technique with multiple apertures. Further significant retirement of system implementation risk could be achieved through demonstrating integration of a full complement of six large apertures and an advanced near-IR fringe tracker at the NPOI facility. Specifically, direct demonstration of the accumulation of errors in the baseline-wavelength bootstrapping system for both wavelength-dependent phenomena (e.g. atmospheric DCR), independent phenomena (e.g. telescope motion), and other terms (e.g. influence of Strehl ratio) would guide design & implementation of a final operational system. Such a system scales naturally from the technology being developed at NPOI: following the framework developed in §3.3, a notional 12×2.3 m system would still have a limiting sensitivity of $m_K = 9.3$ (corresponding to $m_V = 12.3$), with a resolution of 8.9cm at geosynchronous distances.

References

- [1] C. Baranec, R. Riddle, N. M. Law, A. N. Ramaprakash, S. Tendulkar, K. Hogstrom, K. Bui, M. Burse, P. Chordia, H. Das, R. Dekany, S. Kulkarni, and S. Punnaadi. High-efficiency Autonomous Laser Adaptive Optics. *ApJ*, 790:L8, July 2014.
- [2] D. J. Sanchez, S. A. Gregory, D. Werling, T. E. Payne, L. Kann, L. G. Finkner, D. M. Payne, and C. Davis. Photometric measurements of deep space satellites. In J. W. Bilbro, J. B. Breckinridge, R. A. Carreras, S. R. Czyzak, M. J. Eckart, R. D. Fiete, and P. S. Idell, editors, *Imaging Technology and Telescopes*, volume 4091 of *Society of Photo-Optical Instrumentation Engineers (SPIE) Conference Series*, pages 164–182, October 2000.

Table 1: Expected performance of systems with pairwise H -band fringe tracking for N -way B -band imaging: either 3×1.0 m apertures for our forthcoming NPOI upgrade, or 6×0.12 m for NPOI's current apertures; the short H -band baselines in each case are 8m in length. In both cases, switching from an inexpensive InGaAs camera to a higher performance MgCdTe detector enables longer-wavelength K -band fringe tracking, with a ~ 1 magnitude increase in sensitivity.

Parameter	Units	3-way $\times 1.0$ m		NPOI current		Notes
		H -band	B -band	H -band	B -band	
Wavelength	um	1.6	0.44	1.6	0.44	
Aperture size	m	1.00	1.00	0.12	0.12	
Aperture strehl		0.93	0.14	0.95	0.40	
Splits		2	8	2	5	
Integration time	sec	0.040	1.500	0.040	1.500	
Read noise	e rms	35	1	35	1	As appropriate for detector system
Optics temperature	K	290	290	290	290	Ambient room temperature
Optics emissivity		0.46	0.46	0.46	0.46	After 20 reflections at 0.97
Baseline	m	8	56	8	40	$(N_{\text{TEL}} - 1) \times 8$ m for imaging
Object V^2		0.12	0.01	0.12	0.01	For 60mas satellite (e.g. Fig 5)
Throughput to detector		0.54	0.54	0.54	0.54	20 reflections at 0.97
Detector QE		0.7	0.7	0.7	0.7	
Resolution	cm		14.1		19.7	At 35,000 km
SNR		29.4	3.0	36.0	3.0	
Magnitude Limit		8.3	14.7	3.2	10.1	

- [3] A. Müller, J.-U. Pott, S. Morel, R. Abuter, G. van Belle, R. van Boekel, L. Burtscher, F. Delplancke, T. Henning, W. Jaffe, C. Leinert, B. Lopez, A. Matter, K. Meisenheimer, C. Schmid, K. Tristram, and A. P. Verhoeff. First results using PRIMA FSU as a fringe tracker for MIDI. In *Society of Photo-Optical Instrumentation Engineers (SPIE) Conference Series*, volume 7734 of *Society of Photo-Optical Instrumentation Engineers (SPIE) Conference Series*, July 2010.
- [4] E. P. Horch, D. R. Veillette, R. Baena Gallé, S. C. Shah, G. V. O'Rielly, and W. F. van Altena. Observations of Binary Stars with the Differential Speckle Survey Instrument. I. Instrument Description and First Results. *AJ*, 137:5057–5067, June 2009.
- [5] E. P. Horch, L. A. P. Bahi, J. R. Gaulin, S. B. Howell, W. H. Sherry, R. Baena Gallé, and W. F. van Altena. Speckle Observations of Binary Stars with the WIYN Telescope. VII. Measures during 2008-2009. *AJ*, 143:10, January 2012.
- [6] S. Lacour, P. Tuthill, M. Ireland, P. Amico, and J. Girard. Sparse Aperture Masking on Paranal. *The Messenger*, 146:18–23, December 2011.
- [7] J. D. Drummond and R. H. Rast. First Resolved Images of a Spacecraft in Geostationary Orbit with the Keck-II 10 m Telescope. In *The Advanced Maui Optical and Space Surveillance Technologies Conference*, 2010.
- [8] G. van Belle, K. von Braun, J. T. Armstrong, E. K. Baines, H. R. Schmitt, A. M. Jorgensen, N. Elias, D. Mozurkewich, R. Oppenheimer, and S. Restaino. Developing Geostationary Satellite Imaging at the Navy Precision Optical Interferometer. In *Advanced Maui Optical and Space Surveillance Technologies Conference*, page 30, 2015.
- [9] K. Strehl. Über Luftschlieren und Zonenfehler. *Zeitschrift fr Instrumentenkunde*, 22:213–217, July 1902.

- [10] V. N. Mahajan. Strehl ratio for primary aberrations in terms of their aberration variance. *Journal of the Optical Society of America (1917-1983)*, 73:860, 1983.
- [11] A. Glindemann. *Principles of Stellar Interferometry*. Springer-Verlag, 2011.
- [12] J. A. Benson, D. J. Hutter, R. T. Zavala, H. C. Harris, P. D. Shankland, and K. J. Johnston. From fringes to the USNO Navy Prototype Optical Interferometer Astrometric Catalog. In *Society of Photo-Optical Instrumentation Engineers (SPIE) Conference Series*, volume 7734 of *Society of Photo-Optical Instrumentation Engineers (SPIE) Conference Series*, page 3, July 2010.
- [13] J. T. Armstrong, R. B. Hindsley, H. R. Schmitt, F. J. Vrba, J. A. Benson, D. J. Hutter, and R. T. Zavala. Detection of a geostationary satellite with the Navy Prototype Optical Interferometer. In *Society of Photo-Optical Instrumentation Engineers (SPIE) Conference Series*, volume 7734 of *Society of Photo-Optical Instrumentation Engineers (SPIE) Conference Series*, July 2010.
- [14] R. B. Hindsley, J. T. Armstrong, H. R. Schmitt, J. R. Andrews, S. R. Restaino, C. C. Wilcox, J. A. Benson, F. J. Vrba, M. E. DiVittorio, D. J. Hutter, P. D. Shankland, R. T. Zavala, and S. A. Gregory. *Applied Optics*, 50:2692, 2012.
- [15] R. T. Zavala, S. J. Adelman, C. A. Hummel, A. F. Gulliver, H. Caliskan, J. T. Armstrong, D. J. Hutter, K. J. Johnston, and T. A. Pauls. The Mercury-Manganese Binary Star ϕ Herculis: Detection and Properties of the Secondary and Revision of the Elemental Abundances of the Primary. *ApJ*, 655:1046–1057, February 2007.
- [16] M. Hillen, T. Verhoelst, H. Van Winckel, O. Chesneau, C. A. Hummel, J. D. Monnier, C. Farrington, C. Tycner, D. Mourard, T. ten Brummelaar, D. P. K. Banerjee, and R. T. Zavala. An interferometric study of the post-AGB binary 89 Herculis. I. Spatially resolving the continuum circumstellar environment at optical and near-IR wavelengths with the VLTI, NPOI, IOTA, PTI, and the CHARA Array. *A&A*, 559:A111, November 2013.
- [17] E. K. Baines, J. T. Armstrong, H. R. Schmitt, J. A. Benson, R. T. Zavala, and G. T. van Belle. Navy Precision Optical Interferometer Measurements of 10 Stellar Oscillators. *ApJ*, 781:90, February 2014.
- [18] B. Kloppenborg, R. Stencel, J. D. Monnier, G. Schaefer, F. Baron, C. Tycner, R. T. Zavala, D. Hutter, M. Zhao, X. Che, T. ten Brummelaar, C. Farrington, R. Parks, H. McAlister, J. Sturmann, L. Sturmann, P. J. Sallave-Goldfinger, N. Turner, E. Pedretti, and N. Thureau. Interferometry of ϵ Aurigae: Characterization of the asymmetric eclipsing disk. *ArXiv e-prints*, August 2015.
- [19] A. Ghasempour, M. W. Muterspaugh, D. J. Hutter, J. D. Monnier, J. A. Benson, J. T. Armstrong, M. H. Williamson, S. Fall, C. Harrison, and C. Sergeyous. Building the next-generation science camera for the Navy Optical Interferometer. In *Society of Photo-Optical Instrumentation Engineers (SPIE) Conference Series*, volume 8445 of *Society of Photo-Optical Instrumentation Engineers (SPIE) Conference Series*, page 0, July 2012.
- [20] A. M. Jorgensen, D. Mozurkewich, H. R. Schmitt, G. T. van Belle, D. J. Hutter, J. Clark, J. T. Armstrong, E. K. Baines, K. Newman, M. Landavazo, B. Sun, and S. R. Restaino. Progress toward unprecedented imaging of stellar surfaces with the Navy precision optical interferometer.

In *Society of Photo-Optical Instrumentation Engineers (SPIE) Conference Series*, volume 9146 of *Society of Photo-Optical Instrumentation Engineers (SPIE) Conference Series*, page 0, July 2014.

- [21] J. T. Armstrong, A. M. Jorgensen, H. R. Neilson, D. Mozurkewich, E. K. Baines, and H. R. Schmitt. Precise stellar diameters from coherently averaged visibilities. In *Society of Photo-Optical Instrumentation Engineers (SPIE) Conference Series*, volume 8445 of *Society of Photo-Optical Instrumentation Engineers (SPIE) Conference Series*, page 3, July 2012.
- [22] J. T. Armstrong, D. Mozurkewich, L. J. Rickard, D. J. Hutter, J. A. Benson, P. F. Bowers, N. M. Elias, II, C. A. Hummel, K. J. Johnston, D. F. Buscher, J. H. Clark, III, L. Ha, L.-C. Ling, N. M. White, and R. S. Simon. The Navy Prototype Optical Interferometer. *ApJ*, 496:550, March 1998.
- [23] J. T. Armstrong, D. J. Hutter, E. K. Baines, J. A. Benson, R. M. Bevilacqua, T. Buschmann, J. H. Clark, A. Ghasempour, J. C. Hall, R. B. Hindsley, K. J. Johnston, A. M. Jorgensen, D. Mozurkewich, M. W. Muterspaugh, S. R. Restaino, P. D. Shankland, H. R. Schmitt, C. Tyner, G. T. van Belle, and R. T. Zavala. The Navy Precision Optical Interferometer (npoi): AN Update. *Journal of Astronomical Instrumentation*, 2:40002, December 2013.